

Thioether-ligated iron(II) and iron(III)-hydroperoxo/
alkylperoxo complexes with an H-bond donor
in the second coordination sphere†Cite this: *Dalton Trans.*, 2014, **43**,
7522Leland R. Widger,^a Yunbo Jiang,^a Alison C. McQuilken,^a Tzushiung Yang,^a
Maxime A. Siegler,^a Hirotoshi Matsumura,^b Pierre Moënné-Loccoz,^{*b}
Devesh Kumar,^{c,d} Sam P. de Visser^{*c} and David P. Goldberg^{*a}Received 25th January 2014,
Accepted 26th March 2014
DOI: 10.1039/c4dt00281d

www.rsc.org/dalton

The non-heme iron complexes, [Fe^{II}(N3PySR)(CH₃CN)](BF₄)₂ (**1**) and [Fe^{II}(N3Py^{amide}SR)](BF₄)₂ (**2**), afford rare examples of metastable Fe(III)-OOH and Fe(III)-OOtBu complexes containing equatorial thioether ligands and a single H-bond donor in the second coordination sphere. These peroxo complexes were characterized by a range of spectroscopic methods and density functional theory studies. The influence of a thioether ligand and of one H-bond donor on the stability and spectroscopic properties of these complexes was investigated.

Introduction

Iron-(hydro)peroxo and (alkyl)peroxo species are postulated to be critical intermediates in a number of biologically relevant processes, from the utilization of dioxygen for substrate oxidation, to the processing and detoxification of reactive oxygen-derived species (ROS).^{1–5} Some specific examples of non-heme Fe centers involved in this chemistry include isopenicillin N-synthase (IPNS),⁶ superoxide reductase (SOR),⁷ aromatic amino acid hydroxylase (AAH),⁸ Bleomycin,⁹ and cysteine dioxygenase (CDO) (Fig. 1).¹⁰ In one case, the alkylperoxo intermediate of an extradiol ring-cleaving dioxygenase, homoprotocatechuate 2,3-dioxygenase (2,3-HPCD), was structurally characterized by X-ray crystallography.² The physical and spectroscopic properties of these species have been studied in a number of inorganic model complexes,^{11–25} but most of these models utilize only polyamino/polypyridyl ligands. In contrast, some of the enzymes shown in Fig. 1 also

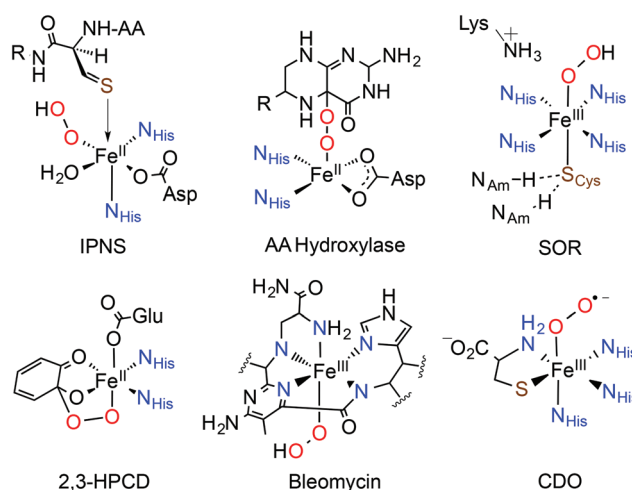


Fig. 1 Selected examples of iron-dioxygen complexes in biology.

^aDepartment of Chemistry, The Johns Hopkins University, 3400 North Charles Street, Baltimore, Maryland 21218, USA. E-mail: dpj@jhu.edu; Fax: +1-410-516-8420; Tel: +1-410-516-6658

^bOregon Health & Science University, Institute of Environmental Health, Mail code: HRC3, 3181 SW Sam Jackson Park Road, Portland, OR 97239, USA. E-mail: moennelo@ohsu.edu; Fax: +1-503-346-3427; Tel: +1-503-346-3429

^cManchester Institute of Biotechnology and School of Chemical Engineering and Analytical Science, The University of Manchester, 131 Princess Street, Manchester, M1 7DN, UK. E-mail: sam.devisser@manchester.ac.uk

^dDepartment of Applied Physics, School of Physical Sciences, Babasaheb, Bhimrao Ambedkar University, Vidya Vihar, Rae Bareilly Road, Lucknow 226-025, India. E-mail: dkclcre@yahoo.com

† Electronic supplementary information (ESI) available: Computational details. CCDC 976172–976174. For ESI and crystallographic data in CIF or other electronic format see DOI: 10.1039/c4dt00281d

include a sulfur donor in the first coordination sphere, but the incorporation of sulfur or other heteroatoms in model complexes is rare.^{23,25–41} In addition, little work has been done to determine the effect of secondary sphere interactions, such as hydrogen-bonding networks, on the structures and spectroscopic properties of iron-peroxo complexes,^{42,43} despite their roles in many of the corresponding enzyme intermediates. Recently our lab has focused on determining the first and second coordination sphere effects on non-heme iron model complexes, including the incorporation of S donors in the first coordination sphere, and oxidizable substrates or H-bond donors in the second coordination sphere.^{44–47}

The thiolate-ligated complex [Fe^{II}(N3PyS)(CH₃CN)]BF₄ was among the first examples of a biomimetic iron(II) complex to

undergo S-oxygenation with O₂ to yield a doubly-oxygenated sulfinate product.⁴⁴ This complex was also useful for studying the fundamental electronic structure and photolability of complexes while employing NO[•] as a surrogate for O₂.⁴⁵ We have examined secondary coordination sphere effects by utilizing the aryl appended complexes, [Fe^{II}(N4Py^{2Ph})(CH₃CN)](BF₄)₂ and [Fe^{II}(N4Py^{amide,2Ph})(CH₃CN)](BF₄)₂. Without a stabilizing H-bond donor positioned near the open site on iron, the alkylperoxo complex [Fe^{III}(N4Py^{2Ph})(OO*t*Bu)]²⁺ likely undergoes rapid O–O bond cleavage to give a putative Fe^{IV}(O) intermediate. The Fe^{IV}(O) would then be situated for attack of the appended aryl group, giving the arene-hydroxylated product. However, in the presence of an amide H-bond donor, [Fe^{III}(N4Py^{amide,2Ph})(OO*t*Bu)]²⁺ is stabilized and only the alkylperoxo-iron(III) complex is observed.⁴⁶ We also determined the influence of first and second coordination sphere modifications in a system in which an equatorial thioether donor was included in the first coordination sphere and an amide H-bond donor was included in the second coordination sphere. The [Fe^{II}(N3Py^{amide}SR)](BF₄)₂ starting material was shown to react with O-atom donors to give [Fe^{IV}(O)(N3Py^{amide}SR)]²⁺ in CH₃CN at –40 °C. This complex is a rare example of a metastable Fe^{IV}(O) complex with a pendant thioether donor, and it does not undergo *intramolecular* oxygen-atom transfer (OAT) to the thioether group. However, this complex does exhibit rapid *intermolecular* OAT to *exogenous* thioether substrates (PhSMe), and it was proposed that amide H-bond donation to the terminal oxo ligand was causing the significant rate accelerations seen for intermolecular OAT.⁴⁷

Herein we report the synthesis and characterization of Fe(III)-OOH and -OO*t*Bu complexes derived from two biomimetic starting compounds, [Fe^{II}(N3PySR)(CH₃CN)](BF₄)₂ (**1**) and [Fe^{II}(N3Py^{amide}SR)](BF₄)₂ (**2**), shown in Scheme 1. These com-

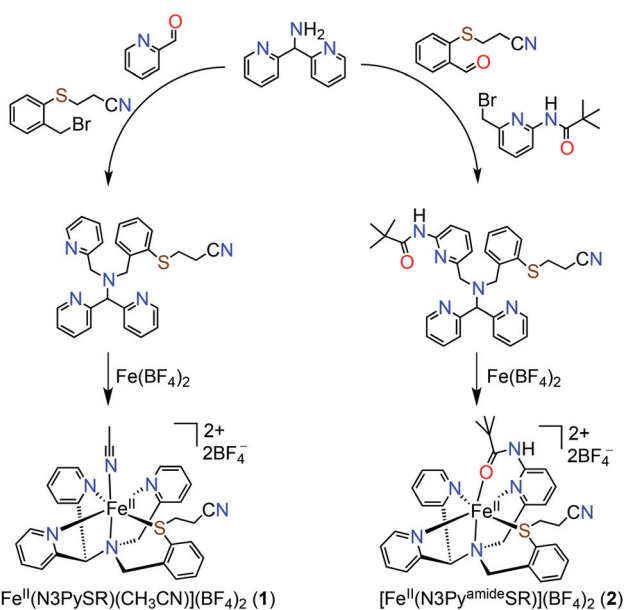
plexes were synthesized by metallation with Fe(BF₄)₂ of their respective purified ligand precursors. Both **1** and **2** possess a thioether ligand in the first coordination sphere, while complex **2** incorporates a single amide N–H group within H-bonding distance of the preferred binding site for anionic ligands. We demonstrate the generation of meta-stable Fe^{III}-OO(H/R) complexes in the presence of the thioether donor ligands starting from **1** and **2**. The influence of a first coordination sphere thioether donor and a second coordination sphere H-bond donor on the stability and spectroscopic properties of the (hydro/alkyl)peroxo iron(III) complexes is assessed.

Results and discussion

Synthesis and characterization

Compound **1** is prepared by metallation of the ligand N3PySR with Fe(BF₄)₂ in MeCN, followed by vapor diffusion of Et₂O into the resulting solution to give dark red blocks of **1** in 68% yield (Scheme 1). The structure of the cation of **1** is shown in Fig. 2 and structural data are summarized in Table 1. The ferrous ion is bound in a pseudo-octahedral geometry by three pyridyl and an aryl thioether donor in the equatorial plane, with a tertiary nitrogen donor and solvent nitrile molecule occupying the axial positions. The Fe–N bond distances (1.9260(14)–1.9969(13) Å, Table 2) are consistent with a low spin (ls) iron(II) center. The spin state was also confirmed by observation of a diamagnetic ¹H-NMR spectrum in CDCl₃.

Metallation of the ligand N3Py^{amide}SR with Fe(BF₄)₂, followed by vapor diffusion of Et₂O into the resulting dark orange solution yielded dark red crystals of **2** in 88% yield. The structure of the cation of **2** (Fig. 3) was reported previously and is repeated here for comparison with the other complexes.⁴⁷ As in **1**, the ferrous ion is low-spin and bound in a pseudo-octahedral geometry with three pyridyl and one aryl thioether donor in the equatorial plane, with the tertiary nitrogen donor occupying the axial position. In **2** however, the amide ligand has displaced the



Scheme 1 Convergent syntheses of **1** and **2**.

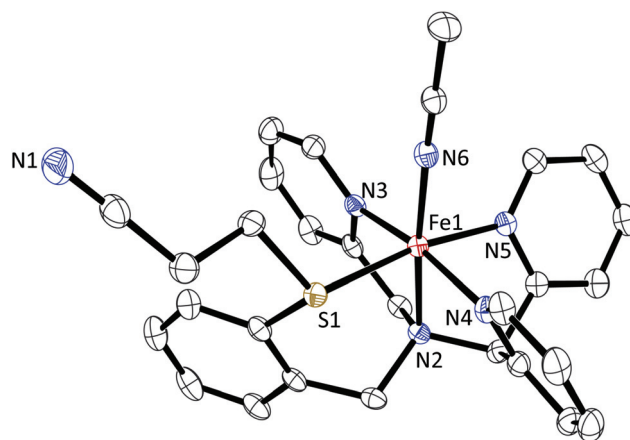


Fig. 2 Displacement ellipsoid plot of the cation of **1** shown at the 50% probability level. H-atoms are removed for clarity.

Table 1 Summary of the crystallographic data for **1**, **3-CH₃CN** and **8**

Complex	1	3-CH₃CN	8
Formula	C ₂₉ H ₂₈ B ₂ F ₈ FeN ₆ S	C ₃₄ H ₃₇ BF _{4.67} FeN ₈ OS	C ₄₄ H ₄₂ B ₂ F ₈ FeN ₆ OS
Formula weight	722.10	761.13	932.37
<i>T</i> (K)	110	110	110
Color, morphology	Dark red, irregular shape	Yellow, lath	Yellow, block
Class	Triclinic	Orthorhombic	Triclinic
Space group	<i>P</i> $\bar{1}$	<i>Pbcn</i>	<i>P</i> $\bar{1}$
<i>a</i> (Å)	10.6689(2)	35.1087(4)	10.4419(3)
<i>b</i> (Å)	12.0355(2)	10.08753(9)	14.5834(3)
<i>c</i> (Å)	13.0403(3)	19.9277(2)	17.2950(4)
α (°)	80.5885(18)	90	90.6304(19)
β (°)	88.0024(18)	90	105.768(2)
γ (°)	68.543(2)	90	106.791(2)
<i>V</i> (Å ³)	1536.85(5)	7057.59(12)	2415.01(10)
ρ (g cm ⁻³)	1.560	1.433	1.282
μ (mm ⁻¹)	0.640	4.546	0.425
(<i>sin</i> θ/λ) _{max} (Å ⁻¹)	0.65	0.62	0.62
No. reflections collected	35 673	44 026	29 736
No. unique reflections	7051	6942	9709
<i>R</i> _{int}	0.0247	0.0273	0.0305
No. variable parameters	425	511	648
<i>R</i> ₁ [<i>I</i> > 2 σ (<i>I</i>)]	0.0325	0.0322	0.0401
<i>wR</i> ₂ [<i>I</i> > 2 σ (<i>I</i>)]	0.0877	0.0791	0.1117
<i>R</i> ₁ [all data]	0.0373	0.0366	0.0475
<i>R</i> ₂ [all data]	0.0905	0.0821	0.1155
Goodness-of-fit (GOF) on <i>F</i> ²	1.061	1.026	1.102
Largest difference in hold and peak (e Å ⁻³)	-0.50, 0.63	-0.33, 0.63	-0.46, 0.58

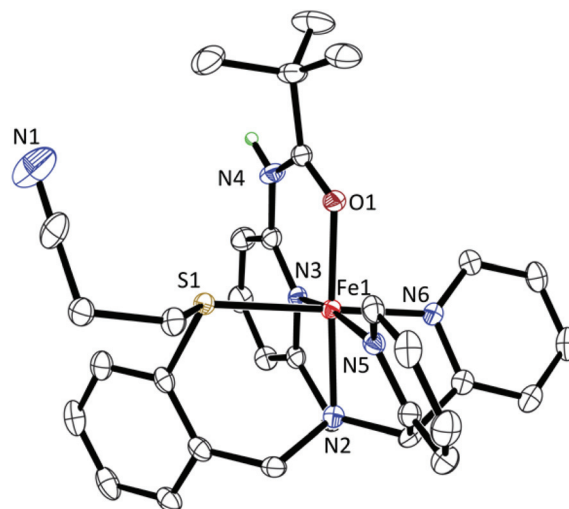
Table 2 Selected bond distances (Å) and angles (°) for **1**

Bond lengths		Bond angles	
Fe1 N6	1.9260(14)	N6 Fe1 N4	94.41(6)
Fe1 N4	1.9569(13)	N6 Fe1 N3	97.35(6)
Fe1 N3	1.9619(13)	N4 Fe1 N3	168.23(6)
Fe1 N5	1.9790(13)	N6 Fe1 N5	94.24(5)
Fe1 N2	1.9969(13)	N4 Fe1 N5	86.41(5)
Fe1 S1	2.2848(4)	N3 Fe1 N5	92.09(5)
		N6 Fe1 N2	175.10(5)
		N4 Fe1 N2	83.35(5)
		N3 Fe1 N2	84.88(5)
		N5 Fe1 N2	81.29(5)
		N6 Fe1 S1	93.13(4)
		N4 Fe1 S1	87.26(4)
		N3 Fe1 S1	92.70(4)
		N5 Fe1 S1	170.63(4)
		N2 Fe1 S1	91.12(4)

bound solvent molecule and is coordinated through the amide oxygen.

When the propionitrile protecting group of the ligand for **1** is removed prior to metal binding, the corresponding Fe^{II}-thiolate complex is accessed, which has been shown to undergo sulfur oxidation in the presence of O₂.⁴⁴ However, in compounds **1** and **2** the thioether donor appears to make these complexes stable toward O₂, with no visible decomposition over several days stored under aerobic conditions.

Prior to attempting to make iron-peroxo complexes from **1** and **2**, we wanted to test the substitution chemistry of **2** toward anionic donors to show that the amide group could be displaced and reoriented into a favorable hydrogen-bonding position. We also wanted to confirm whether hydrogen

**Fig. 3** Displacement ellipsoid plot for the cation of **2** shown at the 50% probability level. H-atoms, except the amide N–H, are removed for clarity. The existence of the H atom attached to N4 was confirmed by difference Fourier map.

bonding would be favored with the anionic ligands found in the axial position. Stirring of **2** with 1.0 equiv. NaN₃ in MeCN, followed by vapor diffusion of Et₂O into the solution produced a small amount of yellow crystals that were manually separated from the bulk precipitate for X-ray structure determination. This structure revealed the new compound, [Fe^{II}(N₃Py^{amide}SR)-(F/N₃)]BF₄ (**3**), which shows that the amide C=O donor has been displaced, and there is a mixture of F⁻ (67%) and N₃⁻ (33%) anions that are occupying the desired axial position.

Table 3 Selected bond lengths (Å) and angles (°) for **3**

Bond lengths		Bond angles	
Fe1 F1	1.850(4)	F1 Fe1 N2	98.05(14)
Fe1 N7	2.063(14)	N7 Fe1 N2	105.6(5)
Fe1 N2	2.1703(16)	F1 Fe1 N1	108.09(14)
Fe1 N1	2.1892(14)	N7 Fe1 N1	102.8(4)
Fe1 N3	2.2012(14)	N2 Fe1 N1	82.68(6)
Fe1 N5	2.2448(13)	F1 Fe1 N3	173.68(12)
Fe1 S1	2.6007(5)	N7 Fe1 N3	176.6(4)
		N2 Fe1 N3	77.62(6)
		N1 Fe1 N3	76.14(5)
		F1 Fe1 N5	98.62(14)
		N7 Fe1 N5	103.3(4)
		N2 Fe1 N5	95.76(5)
		N1 Fe1 N5	153.22(5)
		N3 Fe1 N5	77.41(5)
		F1 Fe1 S1	94.88(14)
		N7 Fe1 S1	87.7(5)
		N2 Fe1 S1	166.53(5)
		N1 Fe1 S1	96.89(4)
		N3 Fe1 S1	89.18(4)
		N5 Fe1 S1	78.52(4)

The Fe–S bond is rather long (2.6007(5) Å), but the sulfur is oriented correctly for a weak bonding interaction with the Fe center (Table 3). The Fe^{II}–N(py) distances (2.1703(16)–2.2448(13) Å) for **3** are indicative of a high-spin (hs) ferrous center, and the difference in Fe–F and Fe–N₃ distances allows for reliable determination of the N₃[−] ligand despite its low occupancy. The N₃[−]-containing component of **3** is shown in Fig. 4, as it more closely resembles the structure of an anionic peroxy ligand than does the F[−] component. The source of fluoride for the F[−]-containing component of **3** can be assigned to BF₄[−]. This structure shows that the axial amide carbonyl is labile, and can be displaced by anionic donors. The structure of **3** also

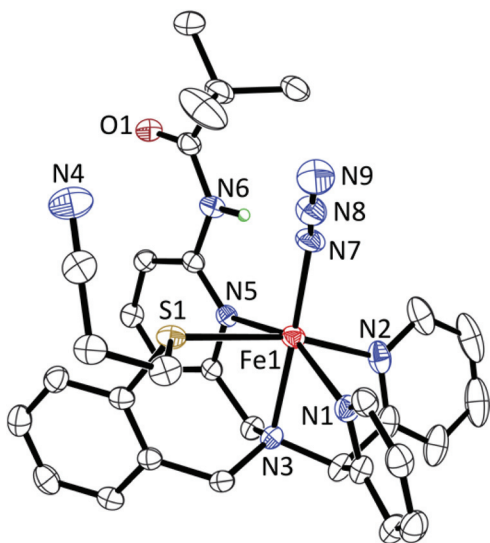


Fig. 4 Displacement ellipsoid plot of the N₃[−]-containing disordered component of the cation of **3** shown at the 50% probability level. H-atoms, except the amide N–H, are removed for clarity. The existence of the H atom attached to N6 was confirmed by difference Fourier map.

shows that the pendant amide is positioned such that H-bonding interactions to anionic ligands are favored (N6...N7 = 2.914(16) Å, N6...F1 = 2.784(5) Å, N6–H–N7 = 174(2)°, N6–H–F1 = 170(2)°; amide N–H is located in the difference map). This complex provides good evidence that Fe–OO(H/R) complexes will likely exhibit the same H-bonding interaction.

Fe^{III}-OOH complexes

Complex **1** reacts with excess H₂O₂ at 25 °C (Fig. 5) to generate a new transient red species, **4** (*t*_{1/2} ≈ 1 min). Monitoring the reaction by UV-vis shows isosbestic conversion of the peaks corresponding to **1** (λ_{max} = 360, 430 nm) into a new spectrum for **4** (λ_{max} = 542 nm, ε = 1000 M^{−1} cm^{−1}). The peak at 542 nm is characteristic of a hydroperoxo-to-iron(III) LMCT band. Attempts to trap this species by generation at −40 °C were unsuccessful, leading only to decomposition, with no observable UV-vis peaks corresponding to **4**. Samples of **4** for analysis by EPR and resonance Raman were therefore prepared at 25 °C and flash-frozen immediately after mixing. From EPR and RR (*vide infra*) complex **4** is assigned as the Fe^{III}-OOH complex [Fe^{III}(OOH)(N3PySR)]²⁺.

Complex **2** reacts with excess H₂O₂ at −40 °C (Fig. 6), and changes in color from orange to deep purple over the course of 30 min. The new purple species (**5**) persists for at least several hours at −40 °C, but immediately decays upon warming to 25 °C. Monitoring by low-temperature UV-vis spectroscopy shows isosbestic conversion from **2** (λ_{max} = 350, 450 nm) to a new peak (λ_{max} = 567 nm, ε = 900 M^{−1} cm^{−1}) that is characteristic of a hydroperoxo-to-iron(III) LMCT band. The EPR and RR spectra (*vide infra*), confirmed that the new species (**5**) is the Fe^{III}-OOH complex, [Fe^{III}(OOH)(N3Py^{amide}SR)]²⁺.

The X-band EPR spectra of **4** and **5** are shown in Fig. 5 and 6, respectively. Both complexes show axial spectra corresponding to 1s iron(III) centers with signals at *g* = 2.17, 2.11,

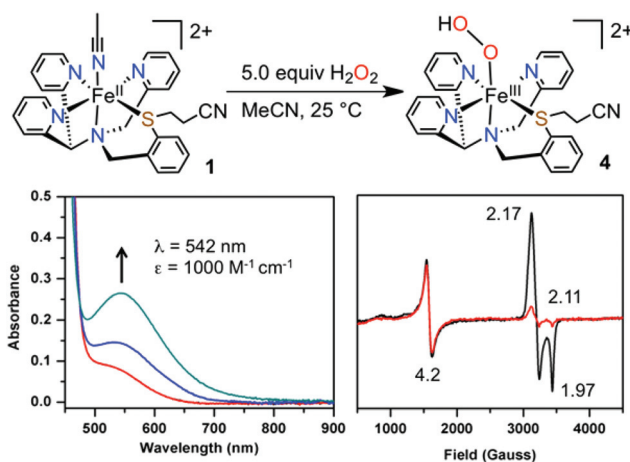


Fig. 5 Formation of [Fe^{III}(OOH)(N3PySR)]²⁺ (**4**) (top). Changes in the electronic absorption spectrum for the reaction of **1** + H₂O₂ in CH₃CN (25 °C), red = **1**, blue = 30 s, green = 60 s (bottom left). X-band EPR spectra of the reaction mixture of **1** + H₂O₂, flash frozen after mixing at 25 °C for 1 min (black line) and 3 min (red line) (bottom right). EPR parameters: *T* = 15 K, frequency = 9.46 GHz, power = 2.01 mW.

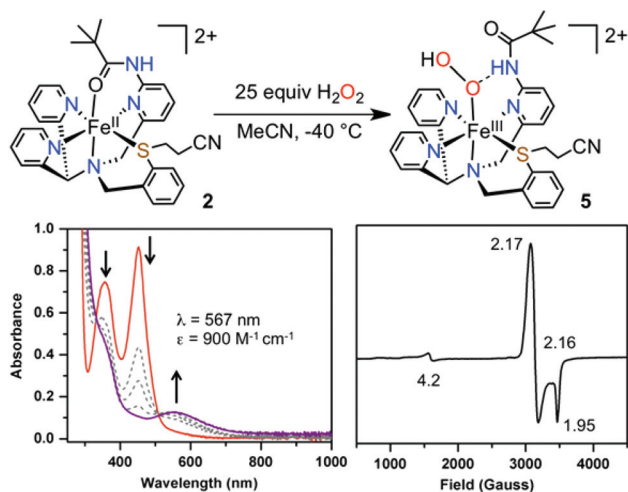


Fig. 6 Formation of [Fe^{III}(OOH)(N3Py^{amide}SR)]²⁺ (**5**) (top). Changes in the electronic absorption spectrum for the reaction of **2** + H₂O₂ in CH₃CN, over 30 min at -40 °C (bottom left). X-band EPR spectrum of the reaction mixture of **2** + H₂O₂, flash frozen after mixing at -40 °C for 30 min. EPR parameters: *T* = 77 K, frequency = 9.46 GHz, power = 2.01 mW.

1.97, for **4** and *g* = 2.17, 2.16, 1.95, for **5**. These values are similar to other Fe^{III}-OOH complexes reported in the literature.¹⁸ The mononuclear complex [Fe^{III}(N4Py)(OOH)]²⁺ in methanol has a signal at *g* = 2.17, 2.12 and 1.97,¹³ while the TPA analogue [Fe^{III}(TPA)(OOH)]²⁺ affords a spectrum with *g* = 2.19, 2.15 and 1.96 in acetone/acetonitrile.⁴⁸ EPR spectra of reaction mixtures of **4**, taken at different timepoints (1–5 min) clearly show the rapid decomposition of the *ls*-Fe^{III} signal at room temperature. Samples frozen after 1 min show a relatively strong *ls*-Fe^{III} signal along with an additional signal at *g* = 4.2. After 3 minutes, the *ls*-Fe^{III} signal appears to be mostly decayed, and after 5 min no *ls*-Fe^{III} signal is observed. The peak at *g* = 4.2 does not increase with the decay of the Fe^{III}-OOH feature, indicating it is not a decomposition product and is likely a byproduct of Fe^{III}-OOH formation. The peak at *g* = 4.2 is much more prominent in **4** relative to that seen in the spectrum of **5**, which was prepared at -40 °C and frozen after 30 min, allowing for full formation of **5** with much less possibility for decay.

The identity of the Fe^{III}-OOH complex **4** was confirmed by RR spectroscopy. Frozen CD₃CN solutions were analyzed at 110 K with a 568 nm laser excitation to avoid overlap of RR bands with non-resonant vibrations from CH₃CN. The RR spectra of **4** show a cluster of bands in the $\nu(\text{Fe-O})$ region with prominent bands at 615, 629, 647 and 664 cm⁻¹, and two bands at 787 and 809 cm⁻¹ in the $\nu(\text{O-O})$ region (Fig. 7A). Labeled samples prepared with H₂¹⁸O₂ exhibit greatly simplified spectra with unique $\nu(\text{Fe-O})$ and $\nu(\text{O-O})$ modes at 590 and 763 cm⁻¹, respectively. RR spectra of samples prepared with D₂O₂ in the presence of excess D₂O also show a single set of $\nu(\text{Fe-O})$ and $\nu(\text{O-O})$ bands at 607 cm⁻¹ and 809 cm⁻¹. These data clearly indicate that the complexity of the RR spectra of unlabeled complex **4** results from vibrational coupling of the

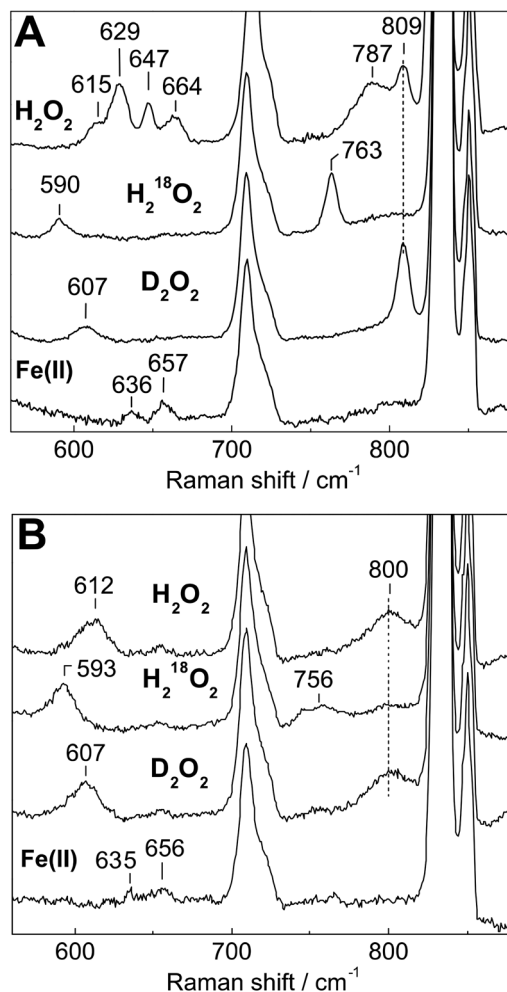


Fig. 7 Resonance Raman spectra of complexes **1** and **4** (A), and **2** and **5** (B) in CD₃CN.

Fe-O-O-H unit with internal vibrations of the (N3PyS) ligand. Using Hooke's law to calculate the $\nu(^{16}\text{O}-^{16}\text{O})$ frequency based on an isolated diatomic oscillator with a $\nu(^{18}\text{O}-^{18}\text{O})$ at 763 cm⁻¹ leads to an 809 cm⁻¹ value that matches the $\nu(\text{O-O})$ mode seen in D₂O and the sharper component of the doublet observed with unlabeled complex **4**. Accordingly, the 809 cm⁻¹ band is assigned to the $\nu(\text{O-O})$ mode of **4**. Using the same approach to interpret the RR bands observed in the $\nu(\text{Fe-O})$ region is less successful,⁴⁹ presumably because of admixture between Fe-O stretch and Fe-O-O bend vibrations, as seen previously with other Fe(III)-hydroperoxo complexes.^{13,50}

The pendant amide complex [Fe^{III}(N3Py^{amide}SR)(OOH)]²⁺ (**5**) was also studied by RR spectroscopy under the same conditions (Fig. 7b). In contrast with **4**, the RR spectra of **5** shows no evidence of vibrational coupling and assigning the $\nu(\text{Fe-O})$ and $\nu(\text{O-O})$ bands is straightforward. The unlabeled complex shows a single $\nu(\text{O-O})$ mode at 800 cm⁻¹ that downshifts to 756 cm⁻¹ with samples prepared with H₂¹⁸O₂ and that is unchanged in samples prepared with D₂O₂ in the presence of excess D₂O. A single band at 612 cm⁻¹ in the $\nu(\text{Fe-O})$ region shifts to 593 cm⁻¹ with H₂¹⁸O₂ and to 607 cm⁻¹ with D₂O₂.

Table 4 Comparison of RR data for 1s non-heme Fe^{III}-OOH complexes

Complex	$\nu(\text{Fe-O}), [\nu(\text{O-O})]$	$\Delta^{18}\text{O}_2$	$\Delta\text{D}_2\text{O}$
$[\text{Fe}^{\text{III}}(\text{N3PySR})(\text{OOH})]^{2+}$	615, [809]	-25, [-46]	-8, [0]
$[\text{Fe}^{\text{III}}(\text{N3Py}^{\text{amide}}\text{SR})(\text{OOH})]^{2+}$	612, [800]	-19, [-44]	-5, [0]
$[\text{Fe}^{\text{III}}(\text{N4Py})(\text{OOH})]^{2+ a}$	632, [790]	-16, [-44]	-5, [0]
$[\text{Fe}^{\text{III}}(\text{TPA})(\text{OOH})]^{2+ b}$	624, [803]	-19, [44]	-3, [0]

^a Ref. 13. ^b Ref. 51.

Comparing $\nu(\text{Fe-O})$ and $\nu(\text{O-O})$ frequencies for **4** and **5** with previously characterized Fe(III)-OOH complexes (Table 4), confirms their identity and suggests that the amide H-bond donor group exerts limited influence on the Fe-O-O unit.

Comparison of the RR data for complexes **4** and **5** with $[\text{Fe}^{\text{III}}(\text{N4Py})(\text{OOH})]^{2+}$ reveals a $19 \pm 2 \text{ cm}^{-1}$ downshift in $\nu(\text{Fe-O})$, and a 10 to 19 cm^{-1} (for **5** and **4**, respectively) upshift of the $\Delta\nu(\text{O-O})$ upon incorporation of the thioether donor. This effect of the equatorial thioether donor on $\nu(\text{O-O})$ differs from a previous study, where the replacement of an axial triflate (OTf^-) ligand with aryl-thiolate donors (ArS^-) in hs $[\text{Fe}^{\text{III}}(\text{Me}_4[15]\text{aneN}_4)(\text{SAr})(\text{OOR})]^+$ complexes was shown to have little influence on $\nu(\text{O-O})$ ($\Delta\nu(\text{O-O}) = 1 \text{ cm}^{-1}$).²³ In contrast, the effect of the equatorial thioether donor on $\nu(\text{Fe-O})$ in **4** and **5** is similar to the effect previously seen for the aryl-thiolate complexes, in which inclusion of sulfur induced a lowering of this band.²³

Fe^{III}-OO*t*Bu complexes

Complex **1** reacts with 10 equiv. of *t*BuOOH (Fig. 8) at -40°C in MeCN to give a new deep blue species (**6**) that persists at low temperature for 15–20 min before slowly decaying. Monitoring the reaction by UV-vis spectroscopy shows the isosbestic conversion of the peaks corresponding to **1**, into a new spectrum ($\lambda_{\text{max}} = 600 \text{ nm}$, $\epsilon = 1670 \text{ M}^{-1} \text{ cm}^{-1}$) that is characteristic of an alkylperoxo-to-iron(III) LMCT band and is in good agreement with similar compounds reported in the literature.^{14,29} The UV-vis spectra reveal that **1** reacts with *t*BuOOH to form **6** within 10 min, but is only stable for a short period and begins to decay after 15 min. The new species (**6**) is assigned as the alkylperoxo complex $[\text{Fe}^{\text{III}}(\text{OO}t\text{Bu})(\text{N3PySR})]^{2+}$.

Complex **2** also reacts with *t*BuOOH at -40°C to give a deep blue solution, similar to that seen for **1**. This new complex (**7**, Fig. 9) is formed *via* isosbestic conversion from **2**, to a new spectrum characteristic for Fe^{III}-OOR complexes ($\lambda_{\text{max}} = 620 \text{ nm}$, $\epsilon = 2000 \text{ M}^{-1} \text{ cm}^{-1}$) within 15 min. As seen for **6**, complex **7** is not stable at -40°C , and slowly decays to a broad, featureless spectrum over 1 h. This species (**7**) is assigned as the ferric-alkylperoxo complex, $[\text{Fe}^{\text{III}}(\text{OO}t\text{Bu})(\text{N3Py}^{\text{amide}}\text{SR})]^{2+}$.

It has been shown that a lowering in energy of peroxo-to-iron(III) charge transfer bands can be correlated with an increasing number of pyridine ligands bound to the iron center, as the π -accepting ability of py ligands lowers the energy of LMCT bands.^{18,52} It is therefore interesting to compare the energy of the LMCT band for compounds **6** and **7**

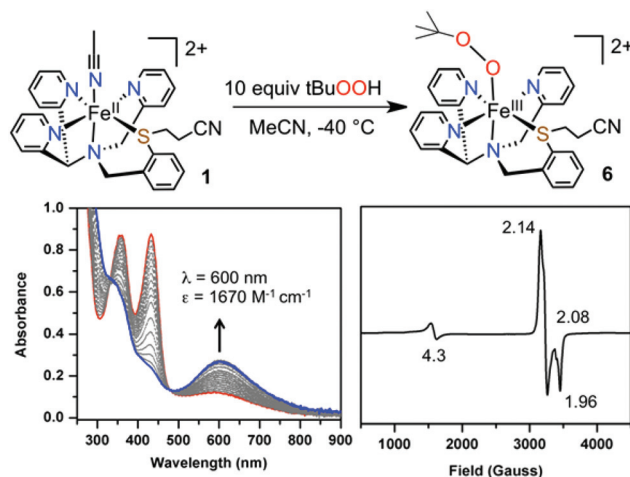


Fig. 8 Formation of $[\text{Fe}^{\text{III}}(\text{OO}t\text{Bu})(\text{N3PySR})]^{2+}$ (**6**) (top). Changes in the electronic absorption spectrum for the reaction of **1** + *t*BuOOH in CH_3CN , over 10 min at -40°C (bottom left). X-band EPR spectrum of the reaction mixture of **1** + *t*BuOOH, flash frozen after mixing at -40°C for 15 min. EPR parameters: $T = 15 \text{ K}$, frequency = 9.46 GHz, power = 2.01 mW.

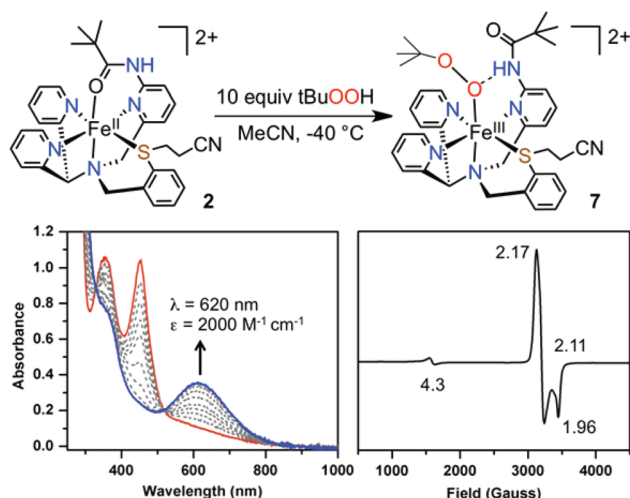


Fig. 9 Formation of $[\text{Fe}^{\text{III}}(\text{OO}t\text{Bu})(\text{N3Py}^{\text{amide}}\text{SR})]^{2+}$ (**7**) (top). Changes in the electronic absorption spectrum for the reaction of **2** + *t*BuOOH in CH_3CN , over 10 min at -40°C (bottom left). X-band EPR spectrum of the reaction mixture of **2** + *t*BuOOH, flash frozen after mixing at -40°C for 15 min. EPR parameters: $T = 77 \text{ K}$, frequency = 9.46 GHz, power = 2.01 mW.

to the parent $[\text{Fe}^{\text{III}}(\text{N4Py})(\text{OO}t\text{Bu})]^{2+}$ compound ($\lambda_{\text{max}} = 560 \text{ nm}$, $\epsilon = 2400 \text{ M}^{-1} \text{ cm}^{-1}$).¹⁵ Relative to N4Py, the thioether-ligated complexes exhibit bands that are shifted to lower energy by 40 nm for **6**, and 60 nm for **7**. These shifts indicate that replacement of a pyridine with a thioether donor causes a significant lowering of the energy of the LMCT band. This change is consistent with stabilization of the metal acceptor orbital caused by the weaker ligand field presented by the thioether donor. In addition, the LMCT bands for both the (hydro) and (alkyl) peroxo-iron(III) complexes are further lowered in energy by the

addition of the H-bond donor, as evidenced by the ~ 20 nm red-shift in the absorption band for both 5 and 7, relative to the non H-bonded 4 and 6.

The X-band EPR spectra for 6 and 7 (Fig. 8 and 9) show that the alkylperoxy species are also low-spin iron(III) with g values of 2.14, 2.08, 1.96 (6), and 2.17, 2.11, 1.96 (7), that are in good agreement with similar compounds previously reported in the literature.^{14,28,29} As seen with the hydroperoxy complexes, spectra of 6 and 7 do show a small peak at $g = 4.3$, consistent with a small amount of high-spin decomposition product.

Resonance Raman spectra of 6 and 7 were collected on frozen samples in CD_3CN at 110 K with a 647 nm laser excitation (Fig. 10). The spectrum of 6 shows two resonance-enhanced vibrations at 700 and 796 cm^{-1} that are in the expected range for $\nu(\text{Fe-O})$ and $\nu(\text{O-O})$, respectively. The RR spectrum of 7 shows similar vibrations at 691 and 796 cm^{-1} .

These $\nu(\text{O-O})$ frequencies below 800 cm^{-1} are consistent with the $1s$ configuration of 6 and 7 and both $\nu(\text{O-O})$ and $\nu(\text{Fe-O})$ closely match reported results for $[\text{Fe}^{\text{III}}(\text{TPA})(\text{OH})_n(\text{OO}t\text{Bu})]^{n+}$ (see Table 5). The presence of the intramolecular H-bond donor in 7 has no effect on the $\nu(\text{O-O})$, but it results in a -9 cm^{-1} downshift of the $\nu(\text{Fe-O})$ relative to 6. RR spectra of complex 7 after H/D exchange of the amide N-H group showed that deuteration of the amide group has no effect on the $\nu(\text{Fe-O})$ and $\nu(\text{O-O})$ signals, which suggests that the H-bonding interaction might be weak. The 7 cm^{-1} downshift of the $\nu(\text{Fe-O})$ in 7, relative to $[\text{Fe}^{\text{III}}(\text{TPA})(\text{OO}t\text{Bu})]^{2+}$, could be due

to changes in Fe-O-O-R angle and level of admixture between Fe-O stretch and Fe-O-O bend rather than changes in Fe-O bond strength.

Density functional theory

Density functional computations at the UB3LYP-D level of theory were utilized to model complexes 4-7 (see ESI† for details). Our initial work explored the spin state ordering of complex 5, for which we calculated the lowest lying doublet (25), quartet (45), and sextet (65) spin states. The doublet spin state was found to be the ground state by 1.5 and 8.5 kcal mol^{-1} over the sextet and quartet spin states, respectively. This spin state ordering reproduces the experimental EPR characterization of 5, which indicates an $S = 1/2$ spin state. Optimized geometries of 25 and 27 are shown in Fig. 11 and are consistent with the proposed structures for complexes 5 and 7, where the iron(III) center is bound in a pseudo-octahedral geometry by the equatorial pyridine and thioether donors, and the tertiary amine and (hydro/alkyl)peroxide ligands occupy the axial positions. The structures also show that the pendant amide H-bond donor has reoriented in both cases, and reveals an $\text{NH}\cdots\text{O}$ hydrogen bond, with calculated N \cdots O distances of 2.774 Å (5) and 2.815 Å (7) and angles of 158.1° (5) and 153.3° (7).

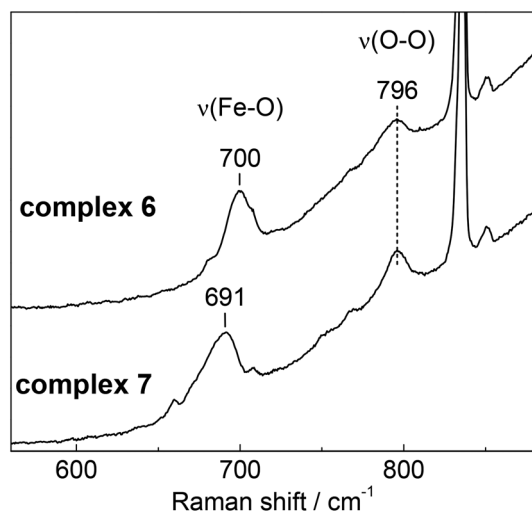


Fig. 10 Resonance Raman spectra of 6 and 7 in CD_3CN .

Table 5 Comparison of RR data for $1s$ non-heme $\text{Fe}^{\text{III}}\text{-OO}t\text{Bu}$ complexes

Complex	$\nu(\text{Fe-O})$	$\nu(\text{O-O})$	Reference
$[\text{Fe}^{\text{III}}(\text{N}3\text{PySR})(\text{OO}t\text{Bu})]^{2+}$	700	796	This work
$[\text{Fe}^{\text{III}}(\text{N}3\text{Py}^{\text{amide}}\text{SR})(\text{OO}t\text{Bu})]^{2+}$	691	796	This work
$[\text{Fe}^{\text{III}}(\text{TPA})(\text{OO}t\text{Bu})]^{2+}$	696	796	22
$[\text{Fe}^{\text{III}}([\text{15}]\text{aneN}_4)(\text{SPh})(\text{OO}t\text{Bu})]^{+}$	612	803	23

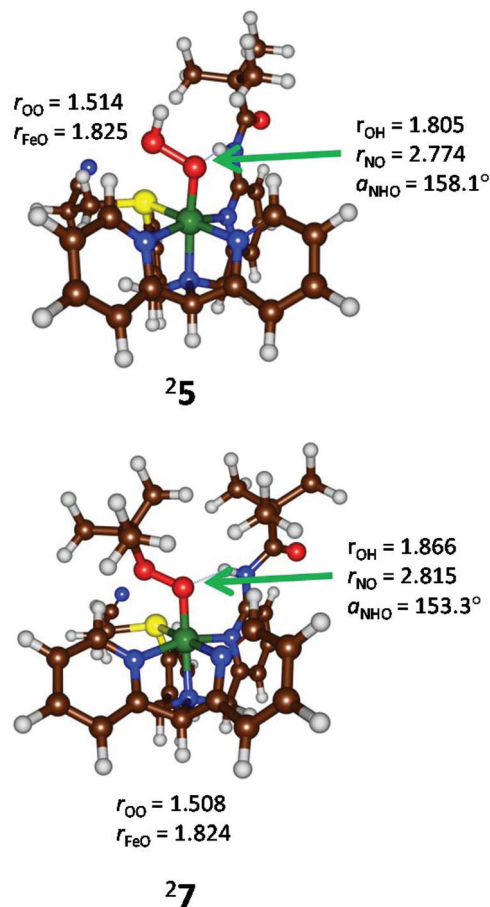


Fig. 11 DFT optimized structures of 25 (top) and 27 (bottom), calculated at the UB3LYP-D level of theory with bond lengths given in angstroms.

Steric influences in the secondary coordination sphere

In further efforts to stabilize the $\text{Fe}^{\text{III}}\text{-OO}(\text{H}/\text{R})$ species, we synthesized the new ligand shown in Scheme 2. The resulting complex, $[\text{Fe}^{\text{II}}(\text{N}3\text{Py}^{\text{amide},2\text{Ph}}\text{SR})](\text{BF}_4)_2$ (**8**), incorporates two phenyl substituents in the second coordination sphere, providing additional steric protection around the putative peroxide binding site (Fig. 12). The synthesis of the $\text{N}3\text{Py}^{\text{amide},2\text{Ph}}\text{SR}$ ligand is shown in Scheme 2. The key synthetic step, incorporation of the phenyl substituents onto the pyridine rings, was accomplished in high yield using Suzuki–Miyaura cross coupling reaction.⁴⁶ Metallation of the free ligand with $\text{Fe}(\text{BF}_4)_2$ was accomplished by stirring in MeCN, and single crystals of **8** were grown from vapor diffusion of Et_2O into the solution. The light yellow crystals reveal Fe–N bond distances (2.1842–2.2267 Å, Table 6) consistent with a high-spin (hs) iron(II) center. As in **2**, the iron(II) ion is bound in a pseudo-octahedral geometry with the 3 pyridine donors and aryl thioether occupying the equatorial positions, while the tertiary amine and the amide carbonyl are bound in the axial positions. The incorporated phenyl substituents are projected orthogonal to

Table 6 Selected bond distances (Å) and angles (°) for **8**

Bond lengths		Bond angles	
Fe1 O1	2.0085(13)	O1 Fe1 N4	83.37(6)
Fe1 N4	2.1842(16)	O1 Fe1 N3	159.27(6)
Fe1 N3	2.1954(15)	N4 Fe1 N3	76.66(6)
Fe1 N1	2.1959(15)	O1 Fe1 N1	111.24(6)
Fe1 N2	2.2267(16)	N4 Fe1 N1	98.60(6)
Fe1 S1	2.6097(5)	N3 Fe1 N1	77.62(6)
		O1 Fe1 N2	120.85(6)
		N4 Fe1 N2	154.51(6)
		N3 Fe1 N2	78.35(6)
		N1 Fe1 N2	80.75(6)
		O1 Fe1 S1	83.97(4)
		N4 Fe1 S1	84.45(4)
		N3 Fe1 S1	88.61(4)
		N1 Fe1 S1	164.70(4)
		N2 Fe1 S1	90.05(4)

the pseudo-equatorial plane, and are oriented to provide significant steric protection around the axial binding site. In contrast to low-spin **1** and **2**, as well as some other hs Fe^{II} complexes,^{28,46} **8** does not react with H_2O_2 or $t\text{BuOOH}$ to afford the corresponding ferric-peroxo complexes, and appears to only undergo outer-sphere oxidation upon addition of a large excess of oxidant (150 equiv.). The lack of reactivity may be due to significant steric encumbrance around the metal center with incorporation of the new phenyl substituents. However, we should point out that the related diphenyl-substituted hs Fe^{II} complex, $[\text{Fe}^{\text{II}}(\text{N}4\text{Py}^{\text{amide},2\text{Ph}})(\text{CH}_3\text{CN})]^{2+}$, does react with $t\text{BuOOH}$ to give an $\text{Fe}^{\text{III}}(\text{OO}t\text{Bu})$ complex at low temperature,⁴⁶ and therefore some additional factors may also be involved in inhibiting the reactivity of **8**.

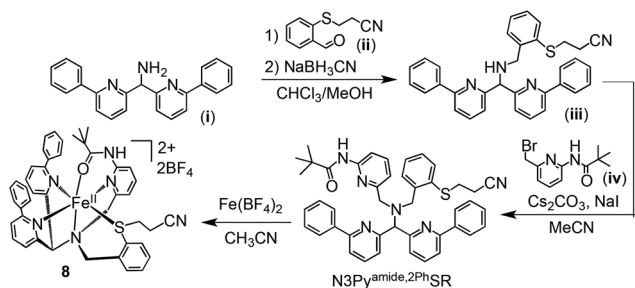
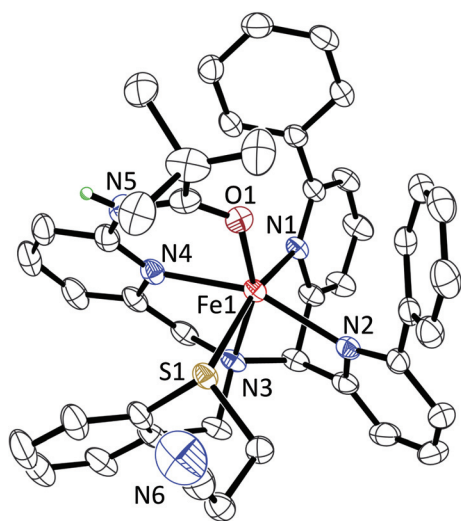
Scheme 2 Synthesis of the ligand precursor ($\text{N}3\text{Py}^{\text{amide},2\text{Ph}}\text{SR}$) to **8**.

Fig. 12 Displacement ellipsoid plot of the cation of **8** shown at the 50% probability level. H-atoms, except the amide N–H, are removed for clarity.

Conclusions

We have synthesized a series of new biomimetic iron(II) model complexes that incorporate a pendant thioether ligand in the equatorial plane. Complexes **1** and **2** react to generate rare examples of Fe^{III} -hydroperoxo and -alkylperoxo complexes with a pendant thioether donor (**4**–**7**). These peroxo species were characterized by UV-vis, EPR and resonance Raman spectroscopy, and DFT calculations supported the proposed structures and spin states. All four peroxo complexes are low-spin species with rhombic EPR resonances centered around $g = 2$, and $\nu(\text{O}-\text{O})$ at $800 \pm 10 \text{ cm}^{-1}$. The hydroperoxo (**4** and **5**) and alkylperoxo (**6** and **7**) complexes show $\nu(\text{Fe}-\text{O})$ at $618 \pm 5 \text{ cm}^{-1}$ and $\nu(\text{Fe}-\text{O})$ at $695 \pm 5 \text{ cm}^{-1}$, respectively, which are also in the expected range for 1s peroxo species. While the addition of an equatorial thioether donor has minimal effects on the alkylperoxo Fe–O–O vibrations, substantial $\nu(\text{Fe}-\text{O})$ and $\nu(\text{O}-\text{O})$ upshifts are seen in the hydroperoxo complexes. The UV-vis data show a significant decrease in the energy of the alkylperoxo-to-iron(III) charge transfer bands, indicating that incorporation of a thioether donor in the first coordination sphere likely stabilizes the key metal acceptor orbital for the LMCT bands in **6** and **7**. Modification of the second coordination

sphere by addition of a single H-bond donor was also shown to affect the properties of these non-heme Fe complexes. Structural characterization of the azide/fluoride-ligated complex **3** showed that the axial amide ligand was indeed labile toward displacement by anionic donors, and that formation of a single hydrogen bond between the amide N–H and anionic ligands in the open site is favored. The inclusion of an amide H-bond donor in the second coordination sphere also appears to shift the peroxo-to-iron LMCT band to lower energy by ~20 nm in both the hydro- and alkylperoxo cases. In contrast, the RR spectra of the peroxo complexes are minimally affected by the addition of the amide H-bond donor. The largest change corresponds to a 9 cm⁻¹ downshift of the $\nu(\text{Fe-O})$ in the Fe^{III}-OO*t*Bu complex **7**. It appears that the addition of the phenyl substituents in **8** inhibits formation of the Fe^{III}-OO(H/R) complexes, and further work is needed to tease out the factors that contribute to this second coordination sphere effect. The results presented here suggest that both first and second coordination sphere effects can be employed by non-heme iron complexes and proteins to subtly tune the reactivity and properties of Fe^{II} and Fe^{III}-OO(H/R) species.

Experimental section

General considerations

All reagents were purchased from commercial vendors and used without further purification unless noted otherwise. The N3PySR ligand⁴⁴ and **2**⁴⁷ were synthesized as previously reported. All reactions were carried out under an atmosphere of N₂ inside a glovebox or under Ar by standard Schlenk and vacuum line techniques. UV-visible spectra were recorded on a Varian Cary 50 spectrophotometer. Electron paramagnetic resonance (EPR) spectra were obtained on a Bruker EMX EPR spectrometer controlled with a Bruker ER 041 XG microwave bridge at 15 or 77 K. The EPR spectrometer was equipped with a continuous-flow liquid He or N₂ cryostat and an ITC503 temperature controller made by Oxford Instruments, Inc. NMR was performed on a Bruker Avance 400 MHz FT-NMR spectrometer at 25 °C. Elemental analysis was performed by Atlantic Microlab Inc., Norcross, GA. LDI-ToF mass spectra were obtained using a Bruker Autoflex III Maldi ToF/ToF instrument (Billerica, MA). Samples were dissolved in CH₂Cl₂ and deposited on the target plate in the absence of any added matrix. Samples were irradiated with a 355 nm UV laser and mass-analyzed by ToF mass spectrometry in the reflectron mode. Resonance Raman spectra were recorded at 110 K using a backscattering geometry with a McPherson 2061/207 spectrograph and a liquid-N₂-cooled CCD camera. The 568 and 647 nm excitations were obtained from a Kr and Ar ion laser, respectively (Innova 300, Coherent). Longpass filters (Razor-Edge, Semrock) were used to attenuate the Raleigh scattering. The samples were kept at 110 K inside a liquid-N₂ coldfinger and spun continuously to prevent photodamage. Frequencies were calibrated relative to an aspirin standard and are accurate to ±1 cm⁻¹. Density functional theory calculations were

performed using previously calibrated and benchmarked methods⁵³ and are explained in detail in the ESI.†

Synthesis of reported compounds

[Fe^{II}(N3PySR)(CH₃CN)](BF₄)₂ (**1**). The free ligand N3PySR (399 mg, 0.89 mmol) was dissolved in CH₃CN (10 mL). A slurry of Fe(BF₄)₂·6H₂O (298 mg, 0.88 mmol) in CH₃CN (10 mL) was added dropwise to the ligand, affording a red suspension. The mixture was allowed to stir for 2 h, and filtered through celite. Diffusion of diethyl ether into a CH₃CN solution afforded dark red blocks after two days. Yield: 409 mg (68%). ¹H NMR (CDCl₃): δ 9.48 (2H), 9.34 (1H), 8.23 (1H), 8.14 (1H), 7.99 (2H), 7.76 (1H), 7.70 (1H), 7.56 (1H), 7.44 (3H), 7.21 (2H), 6.81 (1H), 6.71 (1H), 4.40 (1H), 4.26 (1H), 3.88 (1H), 3.66 (1H), 3.10 (1H), 2.73 (1H), 2.60 (1H). *Anal. Calc.* for C₂₉H₂₈B₂F₈N₆SFe: C, 48.24; H, 3.91; N, 11.64. Found: C, 48.22; H, 3.93; N, 11.70.

[Fe^{III}(N3Py^{amide}SR)(F/N₃)](BF₄)·CH₃CN (F⁻ = 67%, N₃⁻ = 33%) (**3**·CH₃CN). A stock solution of NaN₃ (5.8 mg in 0.5 mL MeOH) was prepared, and 50 μ L of this solution was added to complex **2** (6.5 mg, 9 μ mol) dissolved in 0.5 mL MeCN. Vapor diffusion of Et₂O into the mixture resulted in a small amount of yellow crystals (**3**) suitable for X-ray structure determination, which were separated manually from the bulk material. UV-vis (CH₃CN): λ_{max} = 355, 430 nm, ϵ = 1620, 1680 M⁻¹ cm⁻¹.

[Fe^{III}(N3PySR)(OOH)]²⁺ (**4**). A solution of **1** (0.8 mM) was prepared in MeCN before H₂O₂ (30%, 5.0 equiv.) was added at 25 °C. The yellow solution immediately turned red, then brown. Monitoring by UV-vis (Fig. 5) showed the decay of peaks corresponding to **1** (λ_{max} = 350, 450 nm), with isosbestic conversion to a new spectrum (λ_{max} = 542 nm) that corresponds to **4**. Complex **4** was formed within 60 s and immediately began to decay to a brown species with no prominent UV-vis features. UV-vis: λ_{max} = 542 nm, ϵ = 1000 M⁻¹ cm⁻¹; EPR: g = [2.17, 2.11, 1.97]; RR: $\nu(\text{Fe-O})$ = 615, 629, 647 and 664 cm⁻¹, $\nu(\text{O-O})$ = 809 cm⁻¹.

[Fe^{III}(N3Py^{amide}SR)(OOH)]²⁺ (**5**). An amount of **2** (1.25 mg, 1.7 μ mol) was dissolved in 4.0 mL of MeCN and cooled to -40 °C. A solution of H₂O₂ (0.88 M, 25 equiv., 0.05 mL) in MeCN was added and the color immediately began to change from orange to purple. Monitoring by UV-vis (Fig. 6) revealed full formation of **5** (λ_{max} = 567 nm) within 30 min. UV-vis: λ_{max} = 567 nm, ϵ = 900 M⁻¹ cm⁻¹; EPR: g = [2.17, 2.16, 1.95]; RR: $\nu(\text{Fe-O})$ = 612 cm⁻¹, $\nu(\text{O-O})$ = 800 cm⁻¹.

[Fe^{III}(N3PySR)(OO*t*Bu)]²⁺ (**6**). A solution of **1** (0.8 mM) was prepared in MeCN and cooled to -40 °C. A solution of *t*BuOOH (5.5 M, 10.0 equiv.) diluted in MeCN was added, and the yellow solution immediately turned green, then blue. Monitoring by UV-vis (Fig. 8) showed the peaks corresponding to **1** decay with isosbestic conversion to a new spectrum (λ_{max} = 600 nm) that corresponds to **6**. UV-vis: λ_{max} = 600 nm, ϵ = 1670 M⁻¹ cm⁻¹; EPR: g = [2.14, 2.08, 1.96]; RR: $\nu(\text{Fe-O})$ = 700 cm⁻¹, $\nu(\text{O-O})$ = 796 cm⁻¹.

[Fe^{III}(N3Py^{amide}SR)(OO*t*Bu)]²⁺ (**7**). A solution of **2** (1.1 mM) in MeCN was prepared and cooled to -40 °C. A solution of *t*BuOOH (5.5 M, 10 equiv.) in MeCN was then added and allowed to stir for 20 min. The orange solution of **2** turns

green and finally deep blue, as monitoring by UV-vis (Fig. 9) shows the decay of the peaks corresponding to **2** with the isosbestic growth of a new peak ($\lambda_{\text{max}} = 620 \text{ nm}$) corresponding to **7**. UV-vis: $\lambda_{\text{max}} = 620 \text{ nm}$, $\epsilon = 2000 \text{ M}^{-1} \text{ cm}^{-1}$; EPR: $g = [2.17, 2.11, 1.96]$; RR: $\nu(\text{Fe-O}) = 691 \text{ cm}^{-1}$, $\nu(\text{O-O}) = 796 \text{ cm}^{-1}$.

Secondary amine (iii). Primary amine (**i**)⁴⁶ (825 mg, 2.5 mmol) and aldehyde (**ii**)⁴⁷ (468 mg, 2.5 mmol) were dissolved in a 1 : 1 mixture of CHCl_3 -MeOH (see Scheme 2). Molecular sieves (4 Å) were added and the mixture was stirred under Ar for 48 h. Excess NaBH_3CN (315 mg, 5.0 mmol) was added and allowed to mix for 2 h before being quenched with 1 M HCl. The crude reaction mixture was concentrated, dissolved in CHCl_3 , washed with H_2O , dried and re-concentrated, before being purified on neutral alumina (EtOAc-hexanes) to give 680 mg (53%) of secondary amine **iii** as a pale yellow solid. $^1\text{H-NMR}$ (CDCl_3): δ 8.09–8.07 (m, 4H), 7.72 (t, 2H), 7.63 (d, 2H), 7.54–7.49 (m, 6H), 7.46–7.42 (m, 6H), 5.30 (s, 1H), 4.06 (s, 2H), 3.06 (t, 2H), 2.47 (t, 2H).

$\text{N}_3\text{Py}^{\text{amide},2\text{Ph}}\text{SR}$. Secondary amine (**iii**) (200 mg, 0.4 mmol) and Cs_2CO_3 (196 mg, 0.6 mmol) were combined in 100 mL MeCN, followed by alkyl bromide (**iv**)⁴⁶ (109 mg, 0.4 mmol) and NaI (90 mg, 0.6 mmol) (see Scheme 2). After stirring for 72 h, the crude mixture was filtered through celite and concentrated. The crude solid was dissolved in CHCl_3 , washed with H_2O , dried, and purified by column chromatography on neutral alumina (EtOAc-hexanes) to give 272 mg (97%) of the final ligand as a pale yellow solid. $^1\text{H-NMR}$ (CDCl_3): δ 8.07–8.03 (m, 5H), 7.92–9.90 (m, 2H), 7.73 (t, $J = 8.1 \text{ Hz}$, 2H), 7.67 (dd, $J = 8.8, 1.0 \text{ Hz}$, 2H), 7.60 (t, $J = 7.8 \text{ Hz}$, 2H), 7.50–7.39 (m, 9H), 7.33 (dd, $J = 7.6, 1.5 \text{ Hz}$, 1H), 7.25 (dd, $J = 7.6, 1.3 \text{ Hz}$, 1H), 7.19 (td, 7.5, 1.8 Hz, 1H), 5.53 (s, 1H), 4.29 (s, 2H), 4.06 (s, 2H), 2.94 (t, $J = 7.1 \text{ Hz}$, 2H), 2.37 (t, $J = 7.1 \text{ Hz}$, 2H), 1.31 (s, 9H); $^{13}\text{C NMR}$ (CDCl_3): δ 177.2, 160.1, 159.1, 156.5, 150.8, 141.8, 139.8, 138.7, 137.1, 133.0, 131.4, 130.4, 129.1, 128.9, 127.9, 127.8, 127.3, 123.0, 119.1, 118.8, 118.3, 111.8, 72.0, 57.5, 54.6, 51.9, 40.0, 30.1, 27.8, 18.2, 8.6. FAB-MS (+): $m/z = 703.32127$ [$\text{M} + \text{H}$]⁺ (calcd for $\text{C}_{44}\text{H}_{43}\text{N}_6\text{O}_5$, 703.32191).

$[\text{Fe}^{\text{II}}(\text{N}_3\text{Py}^{\text{amide},2\text{Ph}}\text{SR})_2](\text{BF}_4)_2$ (8**).** The free ligand $\text{N}_3\text{Py}^{\text{amide},2\text{Ph}}\text{SR}$ (461 mg, 0.66 mmol) was dissolved in 5 mL MeCN before $\text{Fe}(\text{BF}_4)_2 \cdot 6\text{H}_2\text{O}$ (221 mg, 0.66 mmol) was added. After stirring for 2 h, the yellow solution was filtered through celite and vapor diffusion of Et_2O gave **8** as yellow crystals suitable for X-ray structure determination (510 mg, 83% yield). $^1\text{H-NMR}$ (CD_3CN): δ 80.67, 65.78, 64.29, 63.25, 53.03, 47.52, 32.37, 24.80, 20.33, 19.42, 13.40, 11.65, 9.19, 8.22, 7.38, 6.22, 4.08, 3.50, 2.33, 1.17, 0.45, -0.45, -2.33, -14.63, -32.73. LDI-MS: $m/z = 757.6$ [$\text{M} - \text{H}$]⁺. UV-vis (CH_3CN): $\lambda_{\text{max}} = 405 \text{ nm}$, $\epsilon = 2650 \text{ M}^{-1} \text{ cm}^{-1}$. Anal. Calc. for [**8**] ($\text{C}_{44}\text{H}_{42}\text{B}_2\text{F}_8\text{FeN}_6\text{O}_5$): predicted: C, 56.68, H, 4.54; N, 9.01; Found: C, 56.53; H 4.72; N, 9.44.

Acknowledgements

The NIH (D.P.G., GM62309 and GM101153, P.M.L. GM074785) is gratefully acknowledged for financial support. The National Service of Computational Chemistry Software (NSCCS) is

thanked for providing cpu time to SdV. H.M. acknowledges support from the JSPS.

Notes and references

- 1 E. G. Kovaleva, M. B. Neibergall, S. Chakrabarty and J. D. Lipscomb, *Acc. Chem. Res.*, 2007, **40**, 475–483.
- 2 E. G. Kovaleva and J. D. Lipscomb, *Science*, 2007, **316**, 453–457.
- 3 E. I. Solomon, A. Decker and N. Lehnert, *Proc. Natl. Acad. Sci. U. S. A.*, 2003, **100**, 3589–3594.
- 4 M. Costas, M. P. Mehn, M. P. Jensen and L. Que, Jr., *Chem. Rev.*, 2004, **104**, 939–986.
- 5 E. I. Solomon, S. D. Wong, L. V. Liu, A. Decker and M. S. Chow, *Curr. Opin. Chem. Biol.*, 2009, **13**, 99–113.
- 6 P. L. Roach, I. J. Clifton, C. M. H. Hensgens, N. Shibata, C. J. Schofield, J. Hajdu and J. E. Baldwin, *Nature*, 1997, **387**, 827–830.
- 7 T. Santos-Silva, J. Trincão, A. L. Carvalho, C. Bonifácio, F. Auchère, P. Raleiras, I. Moura, J. J. G. Moura and M. J. Romão, *J. Biol. Inorg. Chem.*, 2006, **11**, 548–558.
- 8 P. C. A. Bruijninx, G. van Koten and R. J. M. Klein Gebbink, *Chem. Soc. Rev.*, 2008, **37**, 2716–2744.
- 9 L. Que, Jr., *J. Biol. Inorg. Chem.*, 2004, **9**, 684–690.
- 10 S. Ye, X. Wu, L. Wei, D. M. Tang, P. Sun, M. Bartlam and Z. H. Rao, *J. Biol. Chem.*, 2007, **282**, 3391–3402.
- 11 M. J. Vasbinder and A. Bakac, *Inorg. Chem.*, 2007, **46**, 2921–2928.
- 12 G. Roelfes, M. Lubben, K. Chen, R. Y. N. Ho, A. Meetsma, S. Genseberger, R. M. Hermant, R. Hage, S. K. Mandal, V. G. Young, Y. Zang, H. Kooijman, A. L. Spek, L. Que, Jr. and B. L. Feringa, *Inorg. Chem.*, 1999, **38**, 1929–1936.
- 13 G. Roelfes, V. Vrajmasu, K. Chen, R. Y. N. Ho, J.-U. Rohde, C. Zondervan, R. M. la Crois, E. P. Schudde, M. Lutz, A. L. Spek, R. Hage, B. L. Feringa, E. Münck and L. Que, Jr., *Inorg. Chem.*, 2003, **42**, 2639–2653.
- 14 J. Kim, E. Larka, E. C. Wilkinson and L. Que, Jr., *Angew. Chem., Int. Ed.*, 1995, **34**, 2048–2051.
- 15 J.-U. Rohde, S. Torelli, X. P. Shan, M. H. Lim, E. J. Klinker, J. Kaizer, K. Chen, W. Nam and L. Que, Jr., *J. Am. Chem. Soc.*, 2004, **126**, 16750–16761.
- 16 A. Dey and E. I. Solomon, *Inorg. Chim. Acta*, 2010, **363**, 2762–2767.
- 17 A. J. Simaan, S. Döpner, F. Banse, S. Bourcier, G. Bouchoux, A. Boussac, P. Hildebrandt and J.-J. Girerd, *Eur. J. Inorg. Chem.*, 2000, 1627–1633.
- 18 M. Martinho, F. Banse, J. Sainton, C. Philouze, R. Guillot, G. Blain, P. Dorlet, S. Lecomte and J.-J. Girerd, *Inorg. Chem.*, 2007, **46**, 1709–1717.
- 19 A. E. Anastasi, A. Lienke, P. Comba, H. Rohwer and J. E. McGrady, *Eur. J. Inorg. Chem.*, 2007, 65–73.
- 20 M. R. Bukowski, P. Comba, C. Limberg, M. Merz, L. Que, Jr. and T. Wistuba, *Angew. Chem., Int. Ed.*, 2004, **43**, 1283–1287.

- 21 N. Lehnert, R. Y. N. Ho, L. Que, Jr. and E. I. Solomon, *J. Am. Chem. Soc.*, 2001, **123**, 12802–12816.
- 22 N. Lehnert, R. Y. N. Ho, L. Que, Jr. and E. I. Solomon, *J. Am. Chem. Soc.*, 2001, **123**, 8271–8290.
- 23 F. Namuswe, T. Hayashi, Y. B. Jiang, G. D. Kasper, A. A. N. Sarjeant, P. Moënne-Loccoz and D. P. Goldberg, *J. Am. Chem. Soc.*, 2010, **132**, 157–167.
- 24 Y. B. Jiang, J. Telser and D. P. Goldberg, *Chem. Commun.*, 2009, 6828–6830.
- 25 J. Stasser, F. Namuswe, G. D. Kasper, Y. B. Jiang, C. M. Krest, M. T. Green, J. Penner-Hahn and D. P. Goldberg, *Inorg. Chem.*, 2010, **49**, 9178–9190.
- 26 J. Shearer, R. C. Scarrow and J. A. Kovacs, *J. Am. Chem. Soc.*, 2002, **124**, 11709–11717.
- 27 T. Kitagawa, A. Dey, P. Lugo-Mas, J. B. Benedict, W. Kaminsky, E. I. Solomon and J. A. Kovacs, *J. Am. Chem. Soc.*, 2006, **128**, 14448–14449.
- 28 D. Krishnamurthy, G. D. Kasper, F. Namuswe, W. D. Kerber, A. A. N. Sarjeant, P. Moënne-Loccoz and D. P. Goldberg, *J. Am. Chem. Soc.*, 2006, **128**, 14222–14223.
- 29 F. Namuswe, G. D. Kasper, A. A. N. Sarjeant, T. Hayashi, C. M. Krest, M. T. Green, P. Moënne-Loccoz and D. P. Goldberg, *J. Am. Chem. Soc.*, 2008, **130**, 14189–14200.
- 30 K. N. Green, S. M. Brothers, R. M. Jenkins, C. E. Carson, C. A. Grapperhaus and M. Y. Darensbourg, *Inorg. Chem.*, 2007, **46**, 7536–7544.
- 31 C. A. Grapperhaus and M. Y. Darensbourg, *Acc. Chem. Res.*, 1998, **31**, 451–459.
- 32 M. Sallmann, I. Siewert, L. Fohlmeister, C. Limberg and C. Knispel, *Angew. Chem., Int. Ed.*, 2012, **51**, 2234–2237.
- 33 C. S. Mullins, C. A. Grapperhaus, B. C. Frye, L. H. Wood, A. J. Hay, R. M. Buchanan and M. S. Mashuta, *Inorg. Chem.*, 2009, **48**, 9974–9976.
- 34 P. Lugo-Mas, W. Taylor, D. Schweitzer, R. M. Theisen, L. Xu, J. Shearer, R. D. Swartz, M. C. Gleaves, A. DiPasquale, W. Kaminsky and J. A. Kovacs, *Inorg. Chem.*, 2008, **47**, 11228–11236.
- 35 A. C. McQuilken and D. P. Goldberg, *Dalton Trans.*, 2012, **41**, 10883–10899.
- 36 G. Musie, C. H. Lai, J. H. Reibenspies, L. W. Sumner and M. Y. Darensbourg, *Inorg. Chem.*, 1998, **37**, 4086–4093.
- 37 E. Nam, P. E. Alokolaro, R. D. Swartz, M. C. Gleaves, J. Pikul and J. A. Kovacs, *Inorg. Chem.*, 2011, **50**, 1592–1602.
- 38 J. C. Noveron, M. M. Olmstead and P. K. Mascharak, *J. Am. Chem. Soc.*, 2001, **123**, 3247–3259.
- 39 M. G. O'Toole, M. Kreso, P. M. Kozlowski, M. S. Mashuta and C. A. Grapperhaus, *J. Biol. Inorg. Chem.*, 2008, **13**, 1219–1230.
- 40 M. J. Rose, N. M. Betterley, A. G. Oliver and P. K. Mascharak, *Inorg. Chem.*, 2010, **49**, 1854–1864.
- 41 L. A. Tyler, J. C. Noveron, M. M. Olmstead and P. K. Mascharak, *Inorg. Chem.*, 1999, **38**, 616–617.
- 42 D. C. Lacy, J. Mukherjee, R. L. Lucas, V. W. Day and A. S. Borovik, *Polyhedron*, 2013, **52**, 261–267.
- 43 R. L. Shook and A. S. Borovik, *Inorg. Chem.*, 2010, **49**, 3646–3660.
- 44 A. C. McQuilken, Y. B. Jiang, M. A. Siegler and D. P. Goldberg, *J. Am. Chem. Soc.*, 2012, **134**, 8758–8761.
- 45 A. C. McQuilken, Y. Ha, K. D. Sutherlin, M. A. Siegler, K. O. Hodgson, B. Hedman, E. I. Solomon, G. N. L. Jameson and D. P. Goldberg, *J. Am. Chem. Soc.*, 2013, **135**, 14024–14027.
- 46 S. Sahu, L. R. Widger, M. G. Quesne, S. P. de Visser, H. Matsumura, P. Moënne-Loccoz, M. A. Siegler and D. P. Goldberg, *J. Am. Chem. Soc.*, 2013, **135**, 10590–10593.
- 47 L. R. Widger, C. G. Davies, T. Yang, M. A. Siegler, O. Troeppner, G. N. L. Jameson, I. Ivanović-Burmazović and D. P. Goldberg, *J. Am. Chem. Soc.*, 2014, **136**, 2699–2702.
- 48 C. Kim, K. Chen, J. H. Kim and L. Que, Jr., *J. Am. Chem. Soc.*, 1997, **119**, 5964–5965.
- 49 Calculations based on an isolated diatomic oscillator with a $\nu(\text{Fe}^{18}\text{O})$ at 590 cm^{-1} predict a $\nu(\text{Fe}^{16}\text{O})$ at 617 cm^{-1} which does not match any of the most prominent bands seen in the $\nu(\text{Fe-O})$ region of the RR spectra of unlabeled complex **4** nor the 607 cm^{-1} frequency observed in D_2O .
- 50 N. Lehnert, F. Neese, R. Y. N. Ho, L. Que, Jr. and E. I. Solomon, *J. Am. Chem. Soc.*, 2002, **124**, 10810–10822.
- 51 A. M. I. Payeras, R. Y. N. Ho, M. Fujita and L. Que, Jr., *Chem. – Eur. J.*, 2004, **10**, 4944–4953.
- 52 J.-J. Girerd, F. Banse and A. J. Simaan, *Struct. Bonding*, 2000, **97**, 145–177.
- 53 R. Latifi, M. A. Sainna, E. V. Rybak-Akimova and S. P. de Visser, *Chem. – Eur. J.*, 2013, **19**, 4058–4068.